Detection of Air Temperature and Wind Changes Synchronized with the Lamb Wave from the 2022 Tonga Volcanic Eruption

Shingo Watada[1], Yuichi Imanishi[1], and Kenji Tanaka[2]

[1]Earthquake Research Institute, The University of Tokyo

[2]Faculty of Environmental Studies, Hiroshima Institute of Technology

Corresponding author: Shingo Watada (watada@eri.u-tokyo.ac.jp)

Key Points:

- Stacking nation-wide weather network records detects temporal changes in temperature and wind flow synchronized with the Lamb pressure pulse
- Observed temporal variations are close to the adiabatic air compression and Lamb wave flow models expected from the pressure pulse
- Analysis of observed wind speed and pressure changes reveals that the total energy transported by the Lamb pulse was 4.2×10^{16} J

Abstract

The violent 2022 Tonga submarine volcanic eruption produced globally propagating atmospheric disturbance. The short explosive eruption generated a leading Lamb wave pulse that are recorded as a pressure pulse worldwide. A weather station network in Japan recorded the pressure pulse as well as temperature and winds during the passage of the Lamb pressure pulse. Individual temperature and wind records indicate little simultaneous change. However, after aligning temperature and wind records at the timing of pressure pulse arrivals and stacking, we obtain clear temperature and wind changes synchronized with the pressure change. By assuming Lamb wave propagation synthesized temperature and wind changes from the pressure record match well the observed waveforms. Observed wind speed and pressure change of the Lamb pulse directly yield the total energy transported by the pulse to be 4.2×10^{16} J.

Plain Language Summary

Atmospheric disturbance caused by the violent 2022 Tonga volcanic eruption was recorded by multiple types of sensors on the ground. The leading pressure signals, of about 20 min duration and about 2 hPa amplitude, were observed in a nation-wide weather network in Japan as an anomaly that stands out from the background atmospheric pressure trend. Other meteorological sensors such as temperature and wind components were also in operation, but expected changes are on the order of 0.15 K and 0.5 m/s over the 20 min signal duration, too small to be detected in individual records. Using a pressure signal as a time mark for data alignment we averaged all temperature and wind components parallel to the direction from Tonga toward Japan recorded by the network. Such averaging steps greatly reduced the spatially incoherent background noise and enhanced the signals coherent with the arrival of pressure pulse. The resultant temperature and wind changes are comparable to the theoretically predicted ones. The measured temporal changes of atmospheric pressure and air flow enable direct estimation of the energy flow transported by the pressure pulse. The estimated total energy transported by the pressure pulse is between $(3.8—4.6)\times10^{16}$ J.

Index

0350 Atmosphere pressure, density, and temperature

0394 Instrument and techniques

3384 Atmosphere Acoustic-gravity waves

3394 Atmosphere Instruments techniques

8428 Volcano Explosive volcanism

key words,

AMeDAS, meteorological observation network, energy of 2022 Tonga volcanic eruption, temperature and wind of Lamb wave, network stacking, Quantization error and LSB

1 Introduction

The short violent 2022 Tonga submarine (20.536°S, 175.387°W) volcanic eruption on January 15, 2022 around 4:15 (UTC) generated globally propagating impulsive atmospheric pressure waves (Matoza et al., 2022; Vergoz et al., 2022; Wright et al., 2022). The waves were detected by subaerial and submarine pressure sensors (Kubota et al., 2022; Carvajal et al., 2022) as well as other types of sensors such as geostationary meteorological satellite IR-imager as a temperature anomaly of the upper atmosphere (Otsuka, 2022) and ionospheric TEC anomalies in the ground-based GNSS signals (Themens et al., 2022). The leading Lamb wave pressure pulse with a duration of about 20 min propagated around the Earth a few times at the speed of about 300 m/s (Amores et al., 2022; Kubota et al, 2022) and were accompanied by the ground motions that were recorded by seismometers (Poli and Shapiro, 2022). These observations are used to quantify and understand the eruption process.

In addition to pressure, here we report the direct measurements of temperature and wind changes synchronized with the pressure signals recorded by the Automated Meteorological Data Acquisition System (AMeDAS), a nation-wide weather station network in Japan. Given the observed pressure amplitude of about 2 hPa in Japan, if we assume the Lamb wave pressure pulse, we expect that the pressure pulse would be accompanied by a temperature pulse of about 0.15 K and wind anomalies of about 0.5 m/s over the pulse duration of about 20 min. Such small temperature and wind changes are easily masked by the fluctuating background atmospheric conditions and are in fact hardly identified in the individual weather records whereas the pressure pulse from Tonga is distinct (Figure S1). In this paper we introduce a signal enhancement technique synchronized with the pressure signal using networked sensors, and then confirm the detection by comparing observed signals with model predictions, and lastly utilize the temporal profiles of the observed pressure and wind flow to directly estimate the amount of energy transported by the Lamb pulse.

2 Observation

The Japan Meteorological Agency (JMA) operates the AMeDAS network composed of more than 1300 weather stations. Out of these, about 150 stations record air temperature, pressure, wind speed and direction (Figure 1). The 10 s sampling interval is the same for all observational parameters and the quantization steps, i.e., least significant bit (LSB), correspond to 0.1 hPa atmospheric pressure, 0.1 K air temperature, 0.1 m/s wind speed, and 1 degree wind direction. All AMeDAS stations are type JMA-19 equipped with an electronic thermo-hygrometer installed in a vertical cylindrical forced draft ventilator (Daiichi-kagaku, 2022) 1.5 m above the ground. A fan is attached to the top of the cylinder and generates air-flow of 5 m/s from bottom (JMA, 2007) to ease the thermal upheaval by the direct sunshine to the cylinder. Either an ultrasonic or a windmill-type anemometer measures the wind speed and wind direction.

3 Staking AMeDAS records

3.1 Extraction of Lamb wave pulse

After discarding records with a glitch or missing data of the four parameters, i.e., pressure, temperature, wind speed, and wind direction, by visually inspecting four-day-long records starting from January 15 2022 15h UTC, we selected 150 good-quality stations. To extract the Lamb wave pressure signal from the Tonga eruption we remove atmospheric tidal and synoptic and mesoscale variations which are longer than the duration of the Lamb wave pulse of about 20 min by fitting a polynomial function of time to the record and removing it from the record. The residual is dominated by the pressure disturbance from Tonga (Figure 2a, Figure S1). The order of the polynomial is determined by trial and error to balance the signals being removed and remaining. A large polynomial order would almost perfectly remove the long-period trending signal but also partially reduce the signal associated with the Lamb pulse. A small polynomial order would leave long-period signals that are not related to the waves from Tonga in addition to the Lamb pulse. We use 50th order polynomials to extract the Lamb pulse signal from the raw records. Applying a band pass or low-pass filter in the frequency domain is avoided because it tends to create a visible leading artificial siderobe (e.g., Figure 2 of Kubota et al., 2022) with a polarity opposite to the Lamb pulse and such a time-domain artifact could be misinterpreted as a real precursory signal. Causal time domain filters are also avoided because they introduce a frequency-dependent time-shift in the record.

3.2 Measurement of relative time-shift of Lamb pulse

We measure relative time-shifts of the Lamb pulse among the records for network stacking. In the first step we pick the arrival time of each Lamb pulse peak and align the records at the picked time and compute a network-averaged Lamb pulse waveform. In the second step we prepare a one hour long time record of the network-averaged waveform containing the Lamb wave pulse. We compute the cross-correlation function (CCF) between the averaged waveform and each Lamb pulse waveform. The time lag of the maximum CCF peak is a new relative time-shift for network-averaging. Iteratively we can continue the steps to refine the relative time-shift between records by using a new network-averaged waveform but we find that further iterations negligibly change the time lag of the CCF peak. We use the time-shift obtained for each station at the second step for later use.

3.3 Network mean and standard deviation and pressure, temperature and wind records

From the wind speed and wind direction records of each station we construct wind components parallel and tangential to the radial direction from Tonga to the station. To evaluate the Lamb pulse signals in pressure and temperature and wind records embedded in temporal and spatial variations for four days over Japan, we compute the network mean and standard deviation as follows:

$$\bar{f}_i = \frac{1}{4day}\int_0^{4day} f_i(t)dt \qquad (1)$$

$$\hat{f}_i(t) = f_i(t) - \bar{f}_i \qquad (2)$$

$$\bar{f}(t) = \frac{1}{N_{sta}}\sum_{i=1}^{N_{sta}} \hat{f}_i(t + \Delta t_i) \qquad (3)$$

$$\sigma(t) = \sqrt{\frac{\sum_{i=1}^{N_{sta}} \left(\hat{f}_i(t) - \bar{f}(t)\right)^2}{N_{sta}}} \qquad (4)$$

where $f_i(t)$ is either one of original pressure, temperature, radial wind, or tangential wind record of the i-th station. $\bar{f}_i$ is the temporal mean of $f_i(t)$, N_{sta} is the number of stations of the AMeDAS network that we analyze, i.e. 150, $\hat{f}_i(t)$ is the deviation of $f_i(t)$ from the mean, Δt_i is the measured time-shift of the i-th station in section 3.2, $\bar{f}(t)$ is the time-shifted and network-averaged record, $\sigma(t)$ is the standard deviation of $\bar{f}(t)$. Note that $\sigma(t)$ represents a spatial scatter of the signal over the network at time t, not a change of temporal standard deviation over time. We plot $\bar{f}(t)$ and $\sigma(t)$ of pressure, temperature, and radidal wind records of the network in Figure 3.

Since the minor and major arcs from Tonga to a station share the same great circle we note that the time-shift for the major arc path to a station equals to that for the minor arc path with a reversed sign. Therefore stacking the records by using Δt_i measured for the minor arc does not enhance a signal which propagates along the major arc. This is the reason for not detecting the Lamb wave propagated along the major arc in the stacked record (Figure 3c). On the other hand, the first Lamb waves that traveled along the minor arc and the second waves that traveled one more great circle from Tonga to Japan share the same Δt_i, if the time shift is solely due to location of station, and both are enhanced in the stacked record.

The peak-to-peak amplitude of the first Lamb pressure pulse of about 2 hPa (Figure 3f) is comparable to the standard deviation of spatial variation of the pressure over the Japan (Figure 3c). The observed temperature and radial wind signals enhanced by the time alignment (Figures 3e, 3d) are still much smaller than the spatial standard deviation of those. In fact if we take network average without time-shifts temperature and radial wind signals associated with the Lamb wave are completely masked by the background variations (Figures are not shown). The tangential wind component is discussed in section 3.4.

3.4 Network-averaged Lamb pulse in temperature, and wind records

In section 3.1 polynomial filtering was applied to extract the Lamb wave pulse in each pressure record. Here we apply the same polynomial filtering to $\bar{f}(t)$, time-shifted and network averaged pressure, temperature, and radial and tangential winds obtained in section 3.3 and plot a part containing the Lamb wave pulse in Figure 4. Polynomial filtering removes the trend that appeared in Figure 3. The Lamb wave pressure waveform has an amplitude peak of 1.6 hPa followed by negative peaks with amplitudes of about 0.5 hPa (Figure 4d). In the radial wind (Figure 4b) and the temperature (Figure 4c) records we recognize a signal synchronized with the Lamb wave pressure pulse (Figure 4d) but not in the tangential wind (Figure 4a).

Based on the theory of fluid mechanics the wind component parallel to radial direction from Tonga to Japan can be calculated for a given pressure change. The linearized equation of motion of the horizontal momentum balance is given as, e.g. equation (2.1a) of Watada (2009),

$$\rho_0 \frac{\partial u}{\partial t} = -\frac{\partial p'}{\partial x} \qquad (5)$$

where u is the flow velocity of the air in the direction of x, p' is the Eulerian pressure change, ρ_0 is the background air density, x is the horizontal coordinate.

Assuming that u and p' are proportional to $\exp(i(kx - \omega t))$ where k is the horizontal wavenumber and ω is the angular frequency of the Lamb wave, we obtain

$$u = \frac{p'}{\rho_0}\frac{k}{\omega} = \frac{p'}{\rho_0 c} \qquad (6)$$

where $c = \omega/k$ is the horizontal phase velocity of the Lamb wave. The non-dispersive Lamb wave phase velocity is equal to the group velocity, i.e., the propagation speed of the Lamb wave. Figure 4b compares the observed wind flow change in the stacked record and the synthetic wind flow change computed from the pressure change by using equation (6).

The temperature change can be also calculated as follows. When a volume of air of pressure P and temperature T is adiabatically compressed P and T follow (e.g., Bohren and Albrecht, 1998)

$$PT^{\frac{\gamma}{1-\gamma}} = \text{const} \qquad (7)$$

where $\gamma = c_p/c_v$ is the ratio of specific heats, e.g.,1.4 for diatomic gas, c_p and c_v are specific heat capacities of air at constant pressure and volume, respectively. From equation (7) we obtain

$$\left(\frac{dT}{dP}\right)_S = \frac{\gamma - 1}{\gamma}\frac{T}{P}. \qquad (8)$$

Figure 4c compares the observed temperature change in the stacked record and synthetic temperature change computed from the pressure change by using equation (8). For γ, we use the value for dry air since the use of γ for moist air little alters the synthetic change as explained in Text S1.

The synthesized radial wind and temperature variations reproduce the timing, amplitude and duration of the observed radial wind and temperature variations reasonably well, whereas the stacked tangential wind does not show a signature of Lamb wave arrival. This result is consistent with the air flow model of the Lamb wave theory that has no air motion in the tangential direction.

4 Discussions

4.1 Quantization noise

The LSB of temperature record corresponds to a temperature step of 0.1 K. In Figure 4c, however, small temperature variations below 0.1 K in stacked data are well reproduced in the synthesized record. Quantization noise is introduced in the process of quantization of analog data. The quantization noise amplitude distribution can be modeled by a mean of zero and a standard deviation of LSB/$\sqrt{12}$ ≈ 0.3×LSB: (See equation 4.122 of Oppenheim et al., 1999) . This is the reason why the stacked record can resolve a signal smaller than the LSB unit.

4.2 Single station measurement of temperature anomaly in a vault

The observed temperature peak amplitude associated with the Lamb wave is about 0.1K over a duration of 20 min (Figure 4c). Background fluctuation of the atmospheric condition inhibits the detection of such a small temperature change at a single AMeDAS thermometer in the field (Figures 3b, 3e). To confirm the temperature change at a single site we collect environmental monitoring records of the JMA Matsushiro large vault which is under a small

environmental disturbance (c.f. Imanishi, 2022). We find that a pressure variation is comparable to the AMeDAS variation, however, the temperature change is about 0.05 K over a duration of 20 min (Figure S2). The temperature change in the vault is about a half of the AMeDAS variation. The reduced temperature change is likely due to the heat conduction from the air in the vault to the surrounding rocks, soils, and apparatus.

4.3 Measurement of Lamb wave traveling speed and amplitude attenuation

A global average of the Lamb wave traveling speed is measured by the time difference of the traveltimes between the first peak that propagated along the minor arc and the second peak that propagated one more great circle (Figure 3c). The measured traveling speed is 306 m/s.

The wave amplitude decay rate is also measured from the amplitudes of the two Lamb pulses. The amplitude of the Lamb wave traveling on the surface of the Earth is modeled as

$$A\frac{\exp(-\alpha r)}{\sqrt{R\sin\Delta}} \qquad (9)$$

where A is the amplitude factor, R the radius of the Earth, r the traveling distance, Δ the angular distance, α is the decay ratio. From the difference of the traveling distances $r = 40{,}000$ km we obtain $\alpha = 3.06 \times 10^{-5}$/km, which is consistent with the amplitude decays observed globally (Figure 2F of Matoza et al., 2022).

4.4 Variation of the Lamb wave propagation speed

The sound wave speed is controlled by the air temperature , e.g. Amores et al., (2022), and also atmospheric wind e.g. (Figure S28 of Matoza et al., 2022). The time axis of each trace in Figure 2a is reduced so that the arrival time of a wave traveling from Tonga to each station at the speed of 306 m/s would align vertically. Slight misalignments exist in Figure 2a in all azimuth directions. Systematic early arrivals of the Lamb waves up to about 600 sec at stations are noticed (Figure 2c). Especially, the time shifts are enhanced at the sparse southwest stations having smaller azimuths. The time shifts reflect the variations of atmospheric conditions along the Lamb wave paths from Tonga to Japan.

We discuss whether the systematic traveltime anomalies across Japan is possibly explained in a quantitative way without employing rigorous simulation of the traveling Lamb waves in an atmosphere model in which temperature and wind changes temporally and spatially. Based on the atmospheric condition for the eruption day (e.g. Figure 2b) we roughly calculate the expected traveltime delay of the Lamb pulse due to wind and temperature anomalies along the path from Tonga to AMeDAS stations. Detailed steps of the estimating traveltime delay are described in Text S2.

Figure 2b indicates that the strong westerly wind with a more than 40 m/s flow speed at the pressure level of 500 hPa and the cold atmosphere north of 25°N quickly reduce the Lamb pulse traveling speed as it approaches Japan. The delay is expected to be larger in northern Japan. Figure 2c shows an example of delays estimated for an atmospheric model of one time epoch. NCAR/NFL models provide global wind and temperature data in each pressure level four times a day. We compare estimated traveltime delays with the measured relative traveltime delays among AMeDAS stations. The measured trend of early arrivals (plus signs in Figure 2c)

252 in Japan is consistent with estimated trends for the atmosphere models at 300 hPa and 500 hPa
253 isobars. We conclude that the observed traveltime trend of the Lamb pulse will be explained by
254 the temperature and wind models, and sophisticated atmospheric wave propagation simulations
255 for 4D atmosphere models are required to confirm the conclusion.

256 The geostationary meteorological satellite Himawari-8 IR-imager (Murata et al, 2015)
257 captured propagating rings of temperature anomaly with a peak amplitude equivalent to a
258 temperature change by 0.09 K in the upper atmosphere that can be interpreted as the adiabatic
259 temperature change associated with the propagating Lamb pressure wave (Otsuka, 2022). Otsuka
260 (2022) calculated the second order time-derivative of the black body temperature from the full-
261 disk images with the scan interval of 10 min. He noted that the northward propagation of the
262 Lamb wave is slower but the westward propagation is faster than 310 m/s in the northwestern
263 Pacific, consistent with the AMeDAS observation. We reproduce a similar Himawari-8 IR band
264 #8 (wavelength of 6.2 μm) processed image in Figure S6, showing near-Japan region with the
265 scan interval of 2.5 min

266 4.5 Total energy transported by the Lamb pulse

267 The Lamb wave spread out from the Tonga submarine volcano. The wave energy flux
268 transported by an atmospheric wave can be estimated as $\int p\boldsymbol{u}\, dt$, where p is the pressure
269 perturbation and $\boldsymbol{u}$ is the wave flow vector of the atmospheric wave. For radially spreading
270 Lamb waves we can use the observed horizontal flow speed and the pressure change. The well-
271 known vertical scale height of p and $\boldsymbol{u}$ of the Lamb wave allows us to integrate $\rho\boldsymbol{u}$ vertically.
272 The details of estimating the energy transported by the Lamb wave from the Tonga source region
273 is described in Text S3. Two records directly yield an estimate of atmospheric wave energy
274 transported by the Lamb pulse to be between 3.8 and 4.6 $\times 10^{16}$ J, equivalent to the energy
275 between 9.1 and 11 mega ton trinitrotoluene (TNT). Please note that from the measured pressure
276 and wind flow waveforms we directly calculated the energy transported by the Lamb wave, but
277 not the total energy of the eruption that includes other types of wave energy such as short period
278 acoustic waves and slowly propagating gravity waves and seismic waves in addition to thermal
279 and radiation energy. Our energy estimate marks the definite lower bound of the radiated energy
280 from the Tonga eruption. In fact Vergoz et al. (2022) estimated equivalent TNT to be ~100 MT
281 from the characteristic parameters of the Lamb wave (peak amplitude, peak separation time)
282 based on the formula for the nuclear explosion tests.

283

284 **5 Conclusions**

285 The leading Lamb wave pulse, with a peak-to-peak amplitude of about 2 hPa and a peak
286 duration of about 20 min and a triangular time function, and subsequent small amplitude waves
287 were recorded by the atmospheric pressure sensors of the AMeDAS weather network in Japan.
288 Early arrivals of the Lamb waves to southwest Japan by up to about 600 sec relative to those to
289 northern Japan is consistent with traveltime estimates by using wind and temperature models,
290 which predicts slowdown in high latitudes along the paths near Japan. By aligning the
291 temperature records and the wind component records that are parallel to the direction from
292 Tonga to the stations at the arrival time of the Lamb wave pressure, we constructed the network-
293 averaged temperature and radial wind records. The network-averaged records clearly show

changes in temperature and wind speed synchronized with the pressure change of the Lamb wave. Those observed records are close to those theoretically predicted based on the linear wave theory of the Lamb wave and adiabatic compression of the air. By taking advantage of the simple exponential vertical structure of the Lamb wave and cylindrically symmetric spreading from Tonga we evaluated the total energy flow transported by the Lamb pulse that propagated globally. The estimated total energy is (3.8—4.6) $\times 10^{16}$ J which is equivalent to about 10 MT TNT.

Acknowledgments

We thank JMA for operating and maintaining the AMeDAS weather network. This research is funded by JSPS KAKENHI (Grants 19K04034, 21K21353, and 21K18644).

Open Research

The 10 sec AMeDAS network weather station data are purchased from the Japan Meteorological Business Support Center (http://www.jmbsc.or.jp/en/meteo-data.html) by following the purchasing procedures of Non-real-time Dissemination. The satellite image data of Himawari-8 are available from the Japan Aerospace Exploration Agency (JAXA) Earth Observation Research Center (EORC) (https://www.eorc.jaxa.jp/ptree/index.html) after user registration. NCAR GDAS/FNL reanalysis models are available from NCAR Research Data Archive (DOI: 10.5065/D65Q4T4Z) after user registration.

References

Amores, A., Monserrat, S., Marcos, M., Argüeso, D., Villalonga, J., Jordà, G., & Gomis, D. (2022). Numerical simulation of atmospheric Lamb waves generated by the 2022 Hunga-Tonga volcanic eruption. Geophysical Research Letters, 49, e2022GL098240. https://doi.org/10.1029/2022GL098240

Arai, N., Iwakuni, M., Watada, S., Imanishi, Y., Murayama, T., & Nogami, M. (2011). Atmospheric boundary waves excited by the tsunami generation related to the 2011 great Tohoku-Oki earthquake, Geophys. Res. Lett., 38, L00G18. doi:10.1029/2011GL049146

Bohren, C. F., & Albrecht, B. A. (1998). Atmospheric thermodynamics, Oxford University Press, New York.

Carvajal, M., Sepúlveda, I., Gubler, A., & Garreaud, R. (2022). Worldwide signature of the 2022 Tonga volcanic tsunami. Geophysical Research Letters, 49, e2022GL098153. https://doi.org/10.1029/2022GL098153

Daiichi-kagaku (2022). JMA-19 type weather station adopts electronic thermo-hygrometer installed in a vertical forced ventiraton cylinder, Available from: https://www.daiichi-kagaku.co.jp/situdo/weather/amedas (Accessed 26 July 2022)

Goff, J. A., & Gratch, S. (1945). Thermodynamic properties of moist air, Heating, Piping and Air Cond. ASHVE Journal Sect, 17, 334.

Imanishi, Y. (2022). Inertial effects due to eruption-induced atmospheric disturbances identified by superconducting gravimeter observations at Matsushiro, Japan, *Earth, Planets Sp.*, *74*(1). doi:10.1186/s40623-022-01615-4

Japan Meteorological Agency (2007). Weather observation manual, 85, Available from: https://www.jma.go.jp/jma/kishou/know/kansoku_guide/tebiki.pdf (Accessed 26 July 2022)

Kubota, T., Saito, T., & Nishida, K. (2022). Global fast-traveling tsunamis driven by atmospheric Lamb waves on the 2022 Tonga eruption, *Science (80-.).*, *4364*. doi:10.1126/science.abo4364

Lighthill M. J., S. (1978). Waves in fluids, Cambridge University Press. https://ci.nii.ac.jp/ncid/BA00569091

Matoza, R. S. et al. (2022). Atmospheric waves and global seismoacoustic observations of the January 2022 Hunga eruption, Tonga, *Science (80-.).*, (January). doi:10.1126/science.abo7063

Murata, H., Takahashi, M., & Kosaka, Y. (2015). VIS and IR bands of Himawari-8/AHI compatible with those of MTSAT-2/Imager, Meteorological Satellite Center Technical Note, JMA, No. 60, 1-18.

Oppenheim, A. V., Schafer, R. W., & Buck, J. R. (1999). *Discrete-time signal processing*, Prentice Hall signal processing series, 2nd ed., Prentice Hall, Upper Saddle River, New Jersey.

Otsuka, S. (2022). Visualizing Lamb waves from a volcanic eruption using meteorological satellite Himawari-8. Geophysical Research Letters, 49, e2022GL098324. https://doi.org/10.1029/2022GL098324

Poli, P., & Shapiro, N. M. (2022). Rapid characterization of large volcanic eruptions: Measuring the impulse of the Hunga Tonga Ha'apai explosion from teleseismic waves. Geophysical Research Letters, 49, e2022GL098123. https://doi.org/10.1029/2022GL098123

Themens, D. R., Watson, C., Žagar, N., Vasylkevych, S., Elvidge, S., McCaffrey, A., et al. (2022). Global propagation of ionospheric disturbances associated with the 2022 Tonga volcanic eruption. Geophysical Research Letters, 49, e2022GL098158. https://doi.org/10.1029/2022GL098158

Vergoz, J. et al. (2022). IMS observations of infrasound and acoustic-gravity waves produced by the January 2022 volcanic eruption of Hunga, Tonga: A global analysis, *Earth Planet. Sci. Lett.*, *591*, 117639. doi:10.1016/j.epsl.2022.117639

Watada, S. (2009). Radiation of acoustic and gravity waves and propagation of boundary waves in the stratified fluid from a time-varying bottom boundary, *J. Fluid Mech.*, *627*, 361. doi:10.1017/S0022112009005953

Wright, C. J. et al. (2022). Surface-to-space atmospheric waves from Hunga Tonga-Hunga Ha'apai eruption, *Nature*, doi:10.1038/s41586-022-05012-5

Junzeng, X. U., Qi, W. E. I., Shizhang, P. E. N. G., & Yanmei, Y. U. (2012). Error of saturation vapor pressure calculated by different formulas and its effect on calculation of reference evapotranspiration in high latitude cold region, Procedia Engineering, 28, 43-48. doi.org/10.1016/j.proeng.2012.01.680

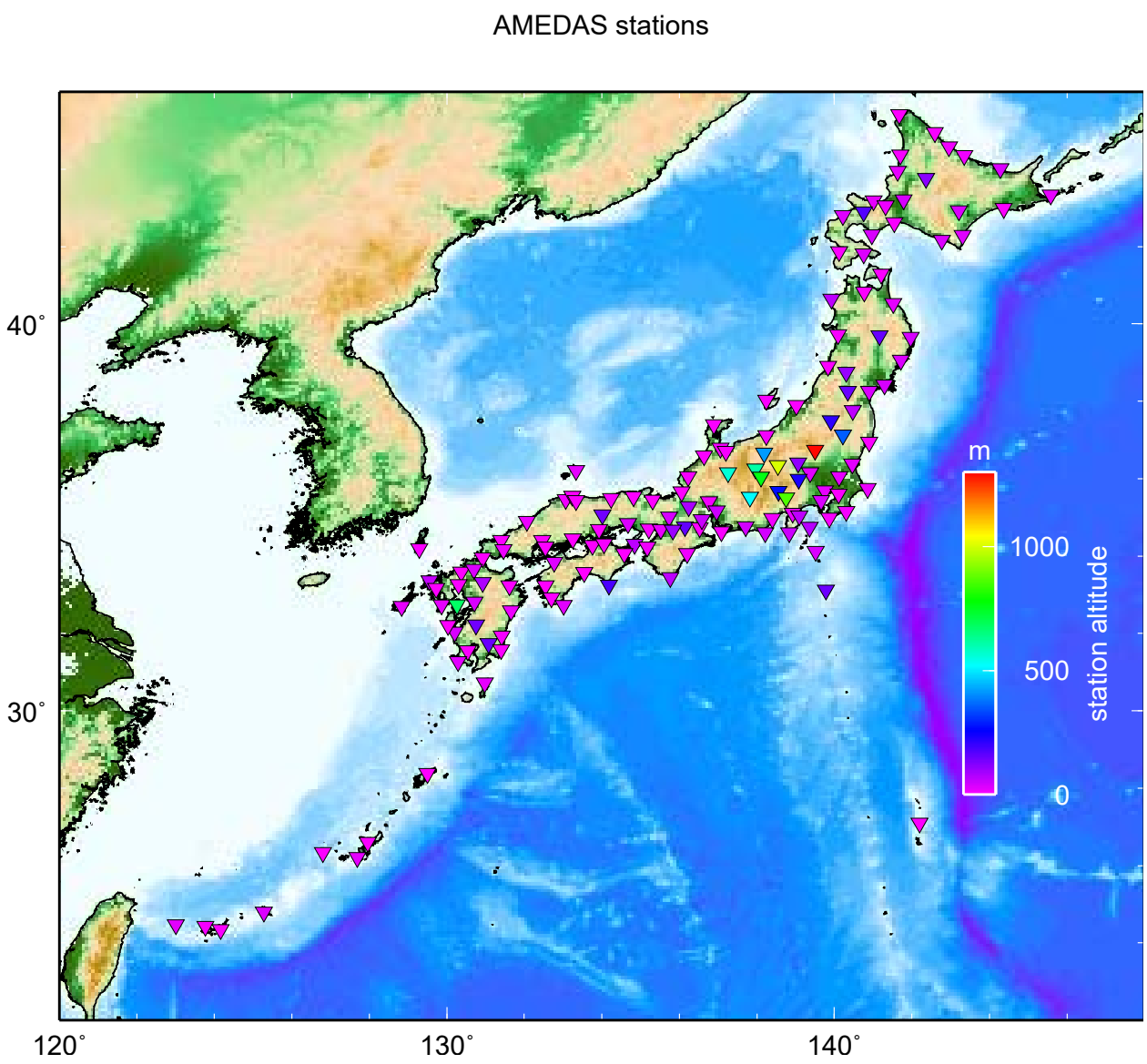

Figure 1.A map of Automated Meteorological Data and Acquisition System (AMeDAS) stations that record pressure, temperature, and wind speed and direction.

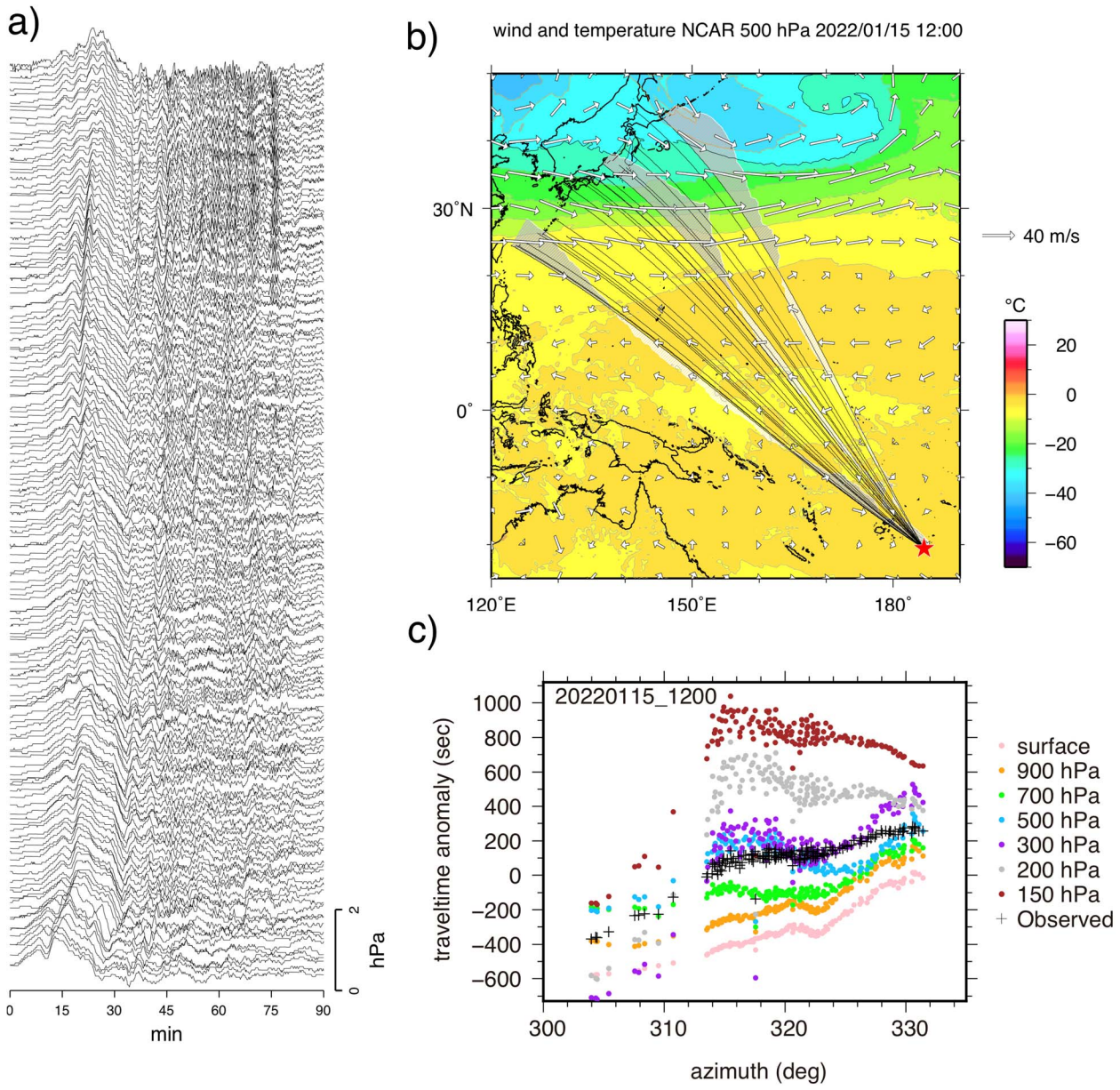

Figure 2. a) Lamb wave pressure pulse recorded at AMeDAS stations. The records are sorted in the order of the station azimuth increasing from bottom to top, i.e., the bottom traces were recorded in southwest Japan and the top traces in northeast Japan. b) Atmospheric temperature and wind velocity of January 15, 2022 at 12h UTC at a pressure level of 500 hPa extracted from the National Center for Atmospheric Research FINAL (NCAR/FNL) reanalysis model. The red star indicates the Tonga submarine volcano. Curved black lines are selected traveling paths to the AMeDAS stations assuming the great circles from Tonga. For better quantification of the wind effect, three paths accompany gray shaded areas and their width indicates the amplitude of head wind component and white shaded areas indicate that of forward wind component of the Lamb pulse propagating toward the stations. c) Colored dots indicate the estimated traveltime delay at each station calculated for the NCAR/FNL model at selected pressure levels. Negative traveltime means that the wave arrives earlier than the global average traveling speed of 306 m/s. Plus (+)

symbols show measured traveltime delays by the waveform (Figure 2a) cross-correlation method. Note that the zero traveltime of measured traveltimes are arbitrary shifted to visually compare with the estimated traveltime. The trend of the traveltime anomaly variations over the azimuth range of AMeDAS stations, not the absolute traveltimes, should be compared with the trend of estimated traveltime anomalies.

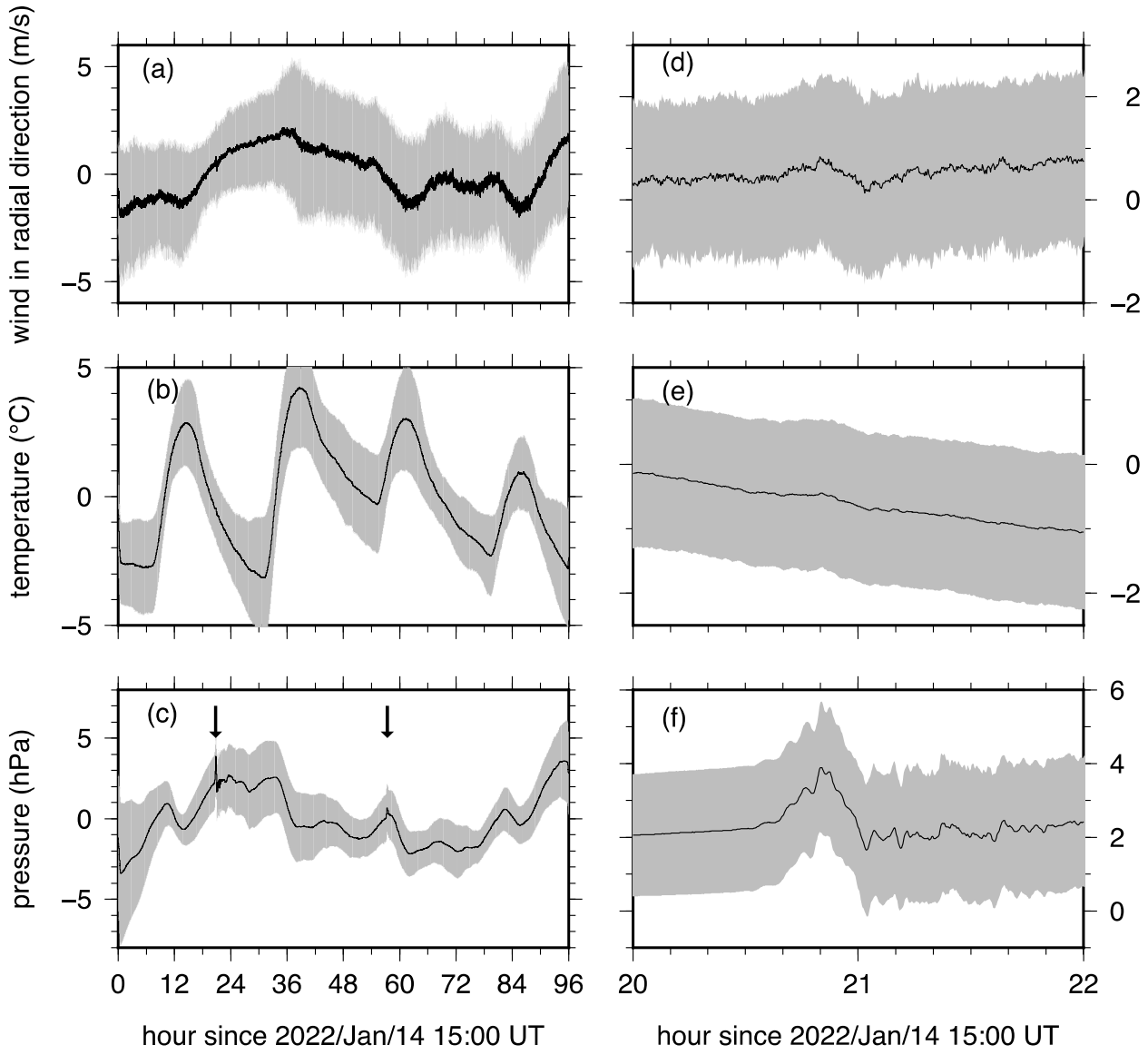

Figure 3. Four-day records of network-averaged (a) radial wind component, (b) temperature, and (c) pressure. The upper bound of the gray area is $\bar{f}(t) + \sigma(t)$ and the lower bounds is $\bar{f}(t) - \sigma(t)$. For all records its mean is first removed (equation 2) so that the 4 day temporal average is zero. Two arrows indicate the arrivals of the Lamb pulse along the minor arc and one more great circle from Tonga. The same time shift Δt_i that is used to stack the pressure record (equation 3) is applied to wind and temperature record for signal enhancement. (d), (e), and (f) are the magnified part of (a), (b), and (c) around the arrival of the first Lamb wave pulse, respectively.

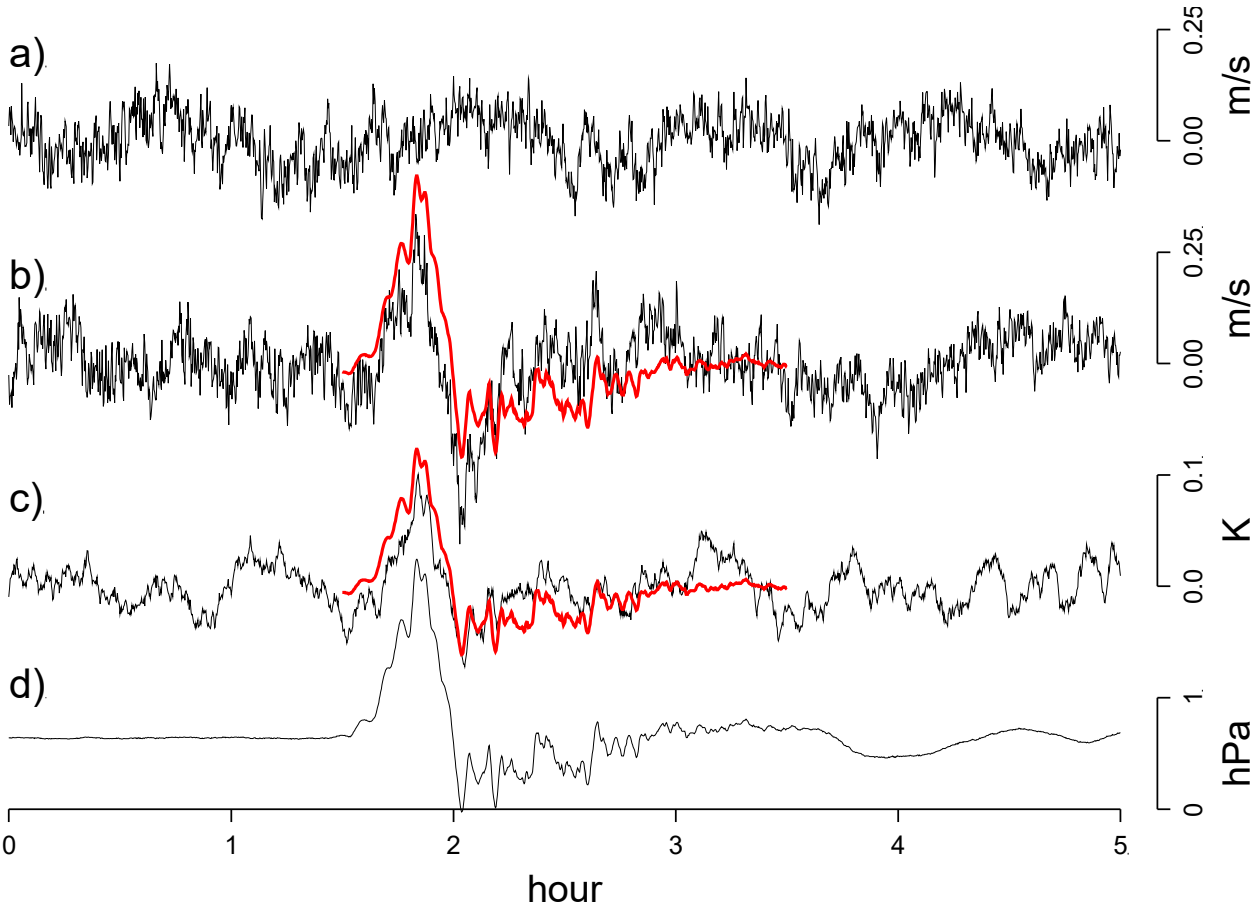

Figure 4. Time-aligned, stacked and filtered (a) tangential wind component, (b) radial wind component, (c) atmospheric temperature, (d) atmospheric pressure records of the AMeDAS network around the first arrival of the Lamb wave pulse. Tangential and radial directions are defined so that the tangential direction is due west when the radial direction is due north. We applied the same polynomial filtering used in section 3.1 to the records in Figures 3d-f and to stacked tangential wind component record (not shown in Figure 3). The red lines in the radial wind component and temperature are synthesized from the pressure record based on the linear equation of motion of fluid (equation 6) and the adiabatic pressure change (equation 8).